J. Fluid Mech. (2019), *vol.* 878, R2, doi:10.1017/jfm.2019.682

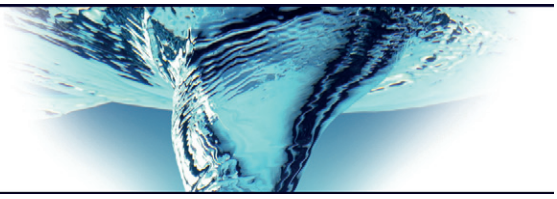

JFM RAPIDS
journals.cambridge.org/rapids

Gliding on a layer of air: impact of a large-viscosity drop on a liquid film

K. R. Langley[1] **and S. T. Thoroddsen**[1,†]

[1]Division of Physical Sciences and Engineering, King Abdullah University of Science and Technology (KAUST), Thuwal, 23955-6900, Saudi Arabia

(Received 4 June 2019; revised 12 August 2019; accepted 13 August 2019;
first published online 6 September 2019)

In this paper we contrast the early impact stage of a highly viscous drop onto a liquid versus a solid substrate. Water drops impacting at low velocities can rebound from a solid surface without contact. This dynamic is mediated through lubrication of a thin air layer between the liquid and solid. Drops can also rebound from a liquid surface, but only for low Weber numbers. Impacts at higher velocities in both cases lead to circular contacts which entrap an air disc under the centre of the drop. Increasing the drop viscosity produces extended air films for impacts on a smooth solid surface even for much larger velocities. These air films eventually break through random wetting contacts with the solid. Herein we use high-speed interferometry to study the extent and thickness profile of the air film for a large-viscosity drop impacting onto a viscous film of the same liquid. We demonstrate a unified scaling of the centreline height of the air film for impacts on both solid and liquid, when using the effective impact velocity. On the other hand, we show that the large-viscosity liquid film promotes air films of larger extent. Furthermore, the rupture behaviour becomes fundamentally different, with the air film between the two compliant surfaces being more stable, lacking the random wetting patches seen on the solid. We map the parameter range where these air films occur and explore the transition from gliding to ring contact at the edge of the drop dimple. After the air film ruptures, the initial contraction occurs very rapidly and for viscosities greater than 100 cSt the retraction velocity of the air film is ~ 0.3 m s^{-1}, independent of the liquid viscosity and impact velocity, in sharp contrast with theoretical predictions.

Key words: drops, breakup/coalescence

1. Introduction

Impacting drops are present and important in many natural and industrial processes and have thus been a research topic of continued interest (Josserand & Thoroddsen

† Email address for correspondence: Sigurdur.Thoroddsen@KAUST.edu.sa

2016). A drop impacting a solid or liquid surface is deformed by the rise in pressure in the intervening gas prior to impact. As the drop deforms, the location of the maximum pressure in the gas layer moves from under the drop centre radially outwards, causing a small disc of air to be entrapped upon contact. In recent years, there have been many studies investigating the physics of the air-disc entrapment for drops impacting solid surfaces (see Thoroddsen *et al.* 2005; Mandre, Mani & Brenner 2009; Hicks & Purvis 2010; Bouwhuis *et al.* 2012; de Ruiter *et al.* 2012; van der Veen *et al.* 2012; Li & Thoroddsen 2015; Philippi, Lagrée & Antkowiak 2016; Langley, Li & Thoroddsen 2017; Li *et al.* 2017; Langley *et al.* 2018).

For low impact velocities, Kolinski, Mahadevan & Rubinstein (2014*a*) and de Ruiter, van den Ende & Mugele (2015) showed that a drop can rebound from even hydrophilic surfaces without contacting the solid surface. Mandre *et al.* (2009) postulated that the surface tension of the drop would stabilize the kink at the edge of the dimple, causing it to skate along the surface, avoiding contact even for high impact velocities, which was inconsistent with the observations of Thoroddsen *et al.* (2005). Kolinski *et al.* (2012) used frustrated total internal reflection to further investigate the skating behaviour and found that the skating behaviour was fleeting, lasting only a few microseconds, and was difficult to observe for drops released from more than 4 cm height.

Taking into consideration the viscosity of the drop, Kolinski, Mahadevan & Rubinstein (2014*b*) found that for impact velocities <1 m s^{-1} and viscosities between 1–100 cSt, the drop initially spreads on top of a thin layer of air. Langley *et al.* (2017) explored a much larger range of viscosities (10–2 $\times$ 10^7 cSt) and velocities (0.3–5.2 m s^{-1}) impacting on smooth solid surfaces, and found that higher-viscosity drops glide over a thin layer of air even at high impact velocities of $\sim$5 m s^{-1}. The thin gliding layer was $<$160 nm thick and the drop could glide for several radii of the initial air disc. During gliding, the air layer ruptured in numerous random locations. The localized contacts initially wet extremely rapidly, grow together, entrapping microbubbles and eventually fully entrapping the central air disc.

Impacts onto liquid films and pools have long been investigated, with many studies focusing on splashing, bouncing, and bubble entrapment due to various mechanisms (see Thoroddsen 2002; Josserand & Zaleski 2003; Thoroddsen, Takehara & Etoh 2003; Howison *et al.* 2005; Yarin 2006; Hicks & Purvis 2011; Marston, Vakarelski & Thoroddsen 2011; Thoroddsen *et al.* 2011, 2012; Tang *et al.* 2018). Tran *et al.* (2013) and Hendrix *et al.* (2016) studied the initial impact dynamics and entrapment of air and found a unified scaling for the entrapped bubble volume for drop impacts onto solid or liquid surfaces, as well as for solid sphere impacts onto liquid pools, that incorporates the number of free interfaces involved in the impact.

The aim of this study is to further probe the gliding behaviour of large-viscosity drops during impacts onto liquid films of the same liquid. Using ultra-high-speed interferometry, we measure the thickness profile of the central air disc, as well as observe the extended gliding followed by the eventual rupture and contraction of the air layer. By impacting a liquid surface, we eliminate possible asperities from the surface, allowing further investigation into the transition between gliding and ring contact at the perimeter of the dimple.

2. Experimental setup

2.1. *Interferometry setup*

The experimental configuration is shown in figure 1(*a*). A viscous drop is expressed from an adjustable height syringe and left to pinch off under the force of gravity. After

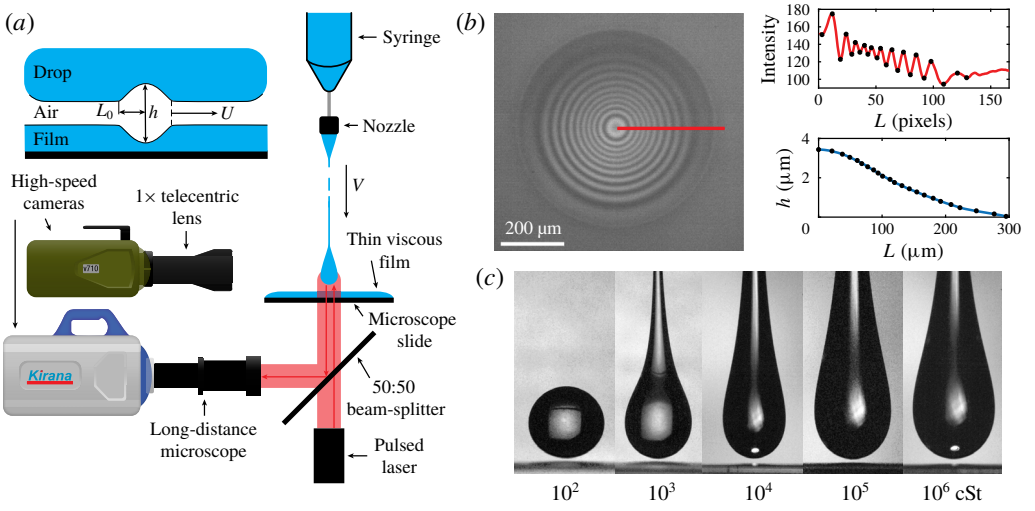

FIGURE 1. (*a*) Sketch of the experimental configuration. A small amount of liquid is deposited onto a microscope slide and allowed to coat uniformly. A small amount of liquid is expressed from an adjustable height syringe and allowed to pinch off under the force of gravity. A Phantom v710 views the impact from the side to measure the velocity of the impact (V) and the bottom radius of curvature of the drop (R_b). The Kirana camera simultaneously captures interference images from below through a beam splitter. The inset in the top left defines several geometric parameters. (*b*) Typical bottom-view interference image. Plots to the right show the averaged intensity profile along the red line in the image (top) and the resulting thickness profile of the air layer (bottom). (*c*) Side-view images showing the drop shapes just prior to impact over the large range of viscosities.

pinch-off, the drop impacts a film of the same liquid that has been deposited onto a clean microscope slide. The camera views the impact through the bottom, using a long-distance microscope (Leica Z16 APO) with adjustable magnification and aperture. Magnifications as large as 29.2 were used, giving a corresponding pixel resolution of up to 1.04 μm px^{-1}. The rapid initial decelerating motions were observed with a high-speed video camera (Kirana-05M, Specialized Imaging, Pitstone, UK) at frame rates up to 5 million f.p.s. (Crooks *et al.* 2013). This camera takes 180 frames each with 924 × 768 px. Video clips were acquired at between 20 and 100 k.f.p.s. to see the longer-term gliding behaviour and between 1 and 5 million f.p.s. to see the rapidly changing early dynamics. The illumination is provided by pulsed laser diodes (SI-LUX640, Specialized Imaging) with a wavelength $\lambda = 640$ nm and adjustable pulse duration set between 70 and 145 ns to minimize motion smearing and provide sufficiently bright illumination. In most cases we use reflective interferometry, with the light coming through the bottom, with a beam splitter, as shown in the sketch. Some imaging was also done with transmission interferometry, where the light comes from the top, to observed better the ruptures. An optical trigger (OT3, Specialized Imaging) intercepts the falling drop from the side and triggers the Kirana camera. The delay between the receipt of the trigger signal and the firing of the camera can be set within the camera software.

As the light emitted upwards from the laser encounters the free surface of the liquid film, some of the light is transmitted and some is reflected. The light transmitted through the first interface traverses the gas film and encounters the surface of the

Fluid	Density ρ (kg m^{-3})	Viscosity μ (cP)	Surface tension σ (dyn cm^{-1})
Air (A) 21 °C	1.2	0.0186	—
Silicone oil 10 cSt	935	9.35	19.8
Silicone oil 100 cSt	965	96.5	20.9
Silicone oil 1000 cSt	970	970	21.2
Silicone oil 10 000 cSt	975	9750	21.5
Silicone oil 100 000 cSt	977	97 700	21.5
Silicone oil 1 000 000 cSt	978	978 000	21.6

TABLE 1. Properties of the fluids used in the experiments. Properties for silicone oil (polydimethylsiloxane) are taken from the supplier's data sheets (Clearco Products).

drop. At this interface, some of the light is again transmitted and some is reflected. The reflected light from the drop interface again traverses the gas film and encounters the free surface of the liquid film, where some is transmitted and some is reflected. The light that is then transmitted through the liquid film after being reflected by the drop surface can interfere with the light reflected initially from the liquid film surface based on the difference in the optical path lengths. Constructive interference is seen as bright fringes and destructive interference is seen as dark fringes with a $\lambda/4$ difference in gas film thickness between adjacent bright and dark fringes. When the light is monochromatic and incident normal to the interface, the intensity in the image, $I(r)$, is given as

$$I(r) \propto \sin^2\left(\frac{\delta(r)\pi}{\lambda/2}\right), \tag{2.1}$$

where r is the radial location and $\delta(r)$ is the air-film thickness, as a function of the radius r from the axis of symmetry. Using the equipment outlined above, this technique can measure a maximum film thickness of $\sim$30 μm when the long-distance microscope is narrowly focused on the liquid free surface; therefore, only the interference due to the intervening air layer is seen in the images, but not the drop surface further from the centre. Figure 1(*b*) shows a typical bottom-view interference image with the extracted intensity profile and the resulting air-layer thickness profile. Typically, monochromatic interferometry can only yield relative measurements of film thicknesses. To overcome this, we use the rapid frame rates to track fringes in time to a point where a known reference height is seen. Herein, we take the point of contact between the drop and liquid film as our reference height of zero.

2.2. *Liquids and drop shapes*

Our experiments focus on the influence of the liquid viscosity and we use silicone oils of viscosities spanning a wide range, between 10 to a million times that of water. Liquid properties are given in table 1. For drops with viscosity >100 cSt, there was a viscous thread attached to the top of the drop, as shown in figure 1(*c*). For most cases, the viscous thread had separated from the nozzle prior to impact; however, in the few cases where the thread was still attached, the resulting effect was a significant reduction in the impact velocity from that expected based on the release height. A separate high-speed camera (Phantom v710) equipped with a 1× telecentric lens (Edmund Optics 55350) views the impact from the side to measure the impact velocity and bottom radius of curvature of the drop.

The impact is on a film of the same liquid ∼400 μm thick. This is done by depositing a fixed amount of liquid (0.55 ± 0.05 g) on the microscope slide, which is then allowed to spread and become of uniform depth.

The thickness of the liquid film was held at an approximately constant level of $T \sim$ 400 μm, except in § 3.4, where it is systematically varied. We did not systematically change the drop radius; however, there is significant variation between the different liquid viscosities, because of the drop oscillations during the free fall differ. This results in values of the bottom radius of curvature of the drop just prior to impact, showing a range of $R_b = 1.4$–3.1 mm. By changing the release height we vary the impact velocity, $V = 0.3$–4.7 m s^{-1}. The liquid viscosities used are shown in table 1. We characterize the impact conditions by the following dimensionless quantities

$$\left.\begin{aligned} Re_\ell = \frac{\rho_\ell R_b V}{\mu_\ell} = 5.2 \times 10^{-4} - 661, \quad We = \frac{\rho_\ell R_b V^2}{\sigma} = 8 - 3120, \\ St = \frac{\mu_g}{\rho_\ell R_b V} = (0.13 - 3.6) \times 10^{-5}, \quad Ca_\ell = \frac{\mu_\ell V}{\sigma} = 0.66 - 1.4 \times 10^5, \end{aligned}\right\} \tag{2.2}$$

where μ_ℓ and σ are the dynamic viscosity and surface tension of the liquid, while in the Stokes number St we use the density of the liquid, ρ_ℓ, balanced by the viscosity of the gas μ_g. The capillary number Ca_ℓ compares the viscous stress in the liquid to the surface tension.

3. Results and discussion

3.1. *Gliding during impact onto a solid versus a liquid*

Figure 2 compares the impact of a 10^5 cSt silicone oil drop on a dry, solid surface with an impact onto a liquid film of the same liquid. The impact velocity and drop size are similar in both cases. For the impact onto a solid surface, there are many localized, random ruptures of the air layer. The thickness of this layer is 160 nm or less, as reported by Langley *et al.* (2017), who used two-colour interferometry to measure the absolute thickness. The local contacts rapidly wet the surface and merge together, sealing off the central air disc.

In contrast, for drops impacting onto liquid films, the drop still glides on an air layer, while the local contacts rarely occur. Instead the air layer ruptures uniformly at some radius, L^*, measured from the centre of the dimple. The example shown in figure 2(*b*) has only a single local contact near the location of the final rupture. This difference is not solely an effect of the smoothness of the liquid versus the solid. Langley *et al.* (2017) performed some impacts onto molecularly smooth mica and found the behaviour to be similar to that shown in figure 2(*a*). The other major difference is the deformability of the liquid surface. This compliance can result in a thicker initial gliding layer, thereby delaying its rupture. Further, as the liquid in the film is displaced by the drop, continuity dictates that the liquid must flow out of the region, resulting in a slightly different boundary condition than for impacts onto solid surfaces.

Aside from the absence of localized contacts in the gliding layer, the two cases also differ in both the time until rupture and the centreline height of the air layer. First, the time to rupture is drastically different. The impact onto a solid has nearly sealed off the air disc in 120 μs from the first deformation of the drop, whereas for the impact onto a liquid film, the rupture occurs after ∼500 μs. The extended time for gliding results in a much larger radius at full rupture for impacts onto a liquid surface:

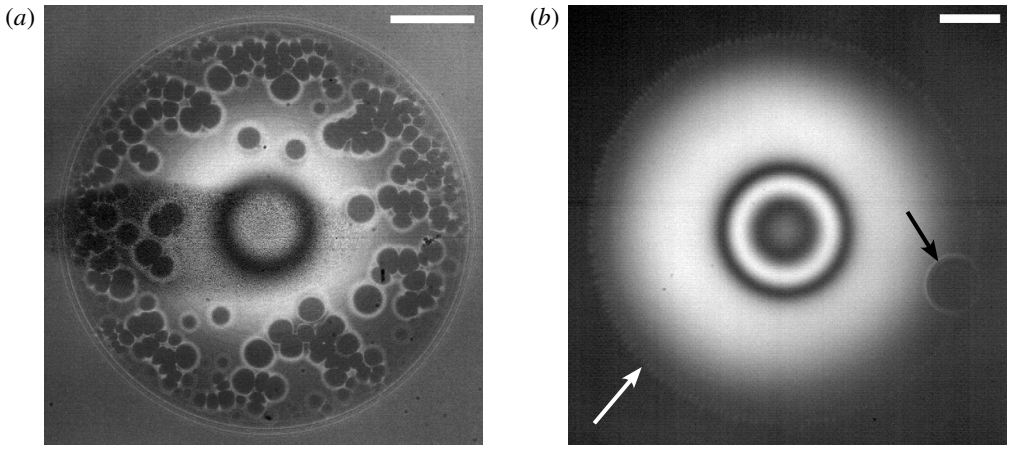

FIGURE 2. Comparison of bottom-view images for impacts of 10^5 cSt silicone oil on a solid versus a liquid surface. (*a*) Impact onto a clean, dry microscope slide at $V = 1.4$ m s^{-1} shown 120 μs after the dimple started to form. The gliding layer is ruptured in numerous random locations that wet extremely fast (Langley *et al.* 2017). (*b*) Impact onto a film of the same 10^5 cSt silicone oil at $V = 1.6$ m s^{-1} shown 500 μs after the dimple is formed. In this case, the drop glides for an extended time, and there is only one localized contact (black arrow) during gliding prior to the simultaneous rupture of the air layer at a uniform radius (white arrow). The scale bar in each image is 200 μm long.

$L^* = 650$ μm for the liquid and $L^* = 330$ μm for the solid, taken as the innermost radius at which the local contacts merge together to fully entrap the air disc. Second, while the rupture of the air film occurs at approximately the same air-film thickness in both cases ($\lesssim$160 nm), the centreline heights of the air disc for these two comparable impact velocities are quite different. The impact onto the liquid film has a centreline height, H_c, nearly 50 % larger. This difference will be discussed in more detail in the following section.

3.2. *Centreline thickness of air layer*

For impacts of an inviscid drop onto a solid surface, the centreline height of the air disc scales as $H_c \sim R_b St^{2/3}$ when compressibility of the gas is unimportant. For values of the compressibility factor $\epsilon < 1$, compressibility becomes important and the initial height of the air layer decreases as a function of ϵ (Mandre *et al.* 2009):

$$\epsilon = P_{atm}\left(\frac{\mu_g}{\rho_\ell^4 V^7 R_b}\right)^{1/3}, \tag{3.1}$$

where P_{atm} is the atmosperic pressure. If the drop is formed instead from a highly viscous liquid, H_c can be much less than the value predicted for the inviscid liquid and the effects of gas compressibility are delayed. Langley *et al.* (2017) found that H_c scales as a function of the impact parameter Φ that takes into account the drop viscosity and inertia and the dynamic pressure forces in the intervening air layer

$$\Phi = \frac{\rho_\ell V^2}{P_{atm}} Re_\ell^{1/3}. \tag{3.2}$$

In the problem at hand, the situation becomes further complicated by the presence of a second deformable interface at the impact surface. Tran *et al.* (2013) found that they could scale drop impacts onto solid and liquid interfaces alike by considering the penetration velocity V_p of the gas film into the substrate instead of just the impact velocity of the drop or solid. They approached the problem from an energy balance, considering the energy before and after impact using the assumption of potential flow and a deep pool to determine the penetration velocity of the drop into the pool to be $V_p = V/2$. This is consistent with other recent studies that consider the velocity of a cavity formed by multiple droplets or jets (Bouwhuis *et al.* 2016; Speirs *et al.* 2018). Hendrix *et al.* (2016) furthered this argument and stated that if one of the interfaces is rigid then $V_p = V$, but for the case of a liquid drop impacting a liquid surface, both interfaces are deformable and $V_p = V/2$. In practice, we do not expect there to be a sharp transition from $V_p = V \to V/2$ as soon as there exists any amount of liquid film beneath the drop, but that there will be a transition region until a deep enough pool is formed. We further discuss the effects of the film thickness in § 3.4.

Herein, we have to consider both the liquid viscosity and a film of finite thickness instead of a deep pool, so the same energy balance arguments used by Tran *et al.* (2013) may not apply here. For the film thickness, we are near the deep pool regime, which is discussed further in § 3.4. From our earlier work (Langley *et al.* 2017), the liquid viscosity has a relatively weak influence on the size of the air disc, and so we persist with using $V_p = V/2$ to find an empirical scaling. However, simply substituting V_p for V in all of the non-dimensional parameters does not yield a consistent scaling for impacts onto both solid and liquid surfaces. We find that using V_p only in the parameters concerning the gas film, namely the Stokes number, which we denote as St_p, collapses the data for impacts onto solid and liquid surfaces. Using the penetration velocity in the Stokes number and the impact velocity elsewhere in the scaling is not without consequences; for example, what happens to the kinematic boundary condition? To fully understand these effects a more rigorous theoretical study is needed.

Figure 3(*a*) presents the centreline height of the air disc as a function of the impact parameter Φ. Open markers are the data collected in this study for impacts onto liquid films. Filled markers represent the data from Langley *et al.* (2017) for impacts onto solid surfaces. In prior studies, H_c was measured when the drop contacted the surface (Li & Thoroddsen 2015) or when the dimple became frozen in time (Langley *et al.* 2017). In this study H_c is more dynamic with time; therefore, the measured values in figure 3(*a*) are taken at the first maximum in the dimple height – see the inset in figure 3(*b*).

As mentioned above, the ordinate is scaled using V_p; however, the abscissa is scaled using V to fully account for the inertia of the drop. In this way, the data for both the impacts onto liquid surfaces and solid surface collapse to the same scaling and the centreline height scales as

$$H_c \sim \Phi^{1/3} R_b St_p^{2/3}. \tag{3.3}$$

(See supplementary materials for alternate scalings, available at https://doi.org/10.1017/jfm.2019.682 using only V or only V_p, which do not work as well.) Thus, H_c is weakly dependent on the viscosity of the liquid drop to the $-1/9$ power. As Φ approaches unity, the initial height of the air film approaches the incompressible, inviscid impact solution. For $\Phi > 1$, viscosity becomes less important while the

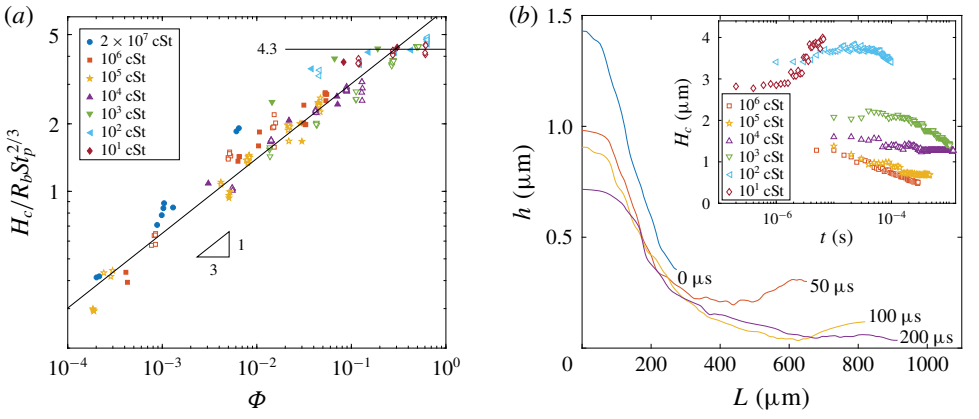

FIGURE 3. (*a*) Plot of the normalized centreline height of the air disc. H_c is measured at the first maximum during the impact, as shown in the inset in (*b*). The open symbols represent impacts onto liquid films and the filled symbols represent impacts onto solid surfaces from Langley *et al.* (2017). Using the penetration velocity of the gas film in the Stokes number, the data for impacts onto liquid surfaces scale in accordance with the scaling for impacts onto solid surfaces. In both cases the centreline height is weakly dependent on the liquid viscosity to the $-1/9$ power. (*b*) Half-profiles of the air-layer thickness at several times for a 10^5 cSt silicone oil drop impacting at $V = 1.6$ m s^{-1} ($\Phi = 7.8 \times 10^{-3}$). Time is measured from the first frame in which the dimple is visible. Inset: Centreline height of the air disc from the first appearance of the dimple until air film rupture for each viscosity used herein, for impact velocities of 2.0 m s^{-1} (10 cSt), 1.9 m s^{-1} (100 cSt, 10^6 cSt), 1.8 m s^{-1} (10^3 cSt), 1.6 m s^{-1} (10^4 cSt, 10^5 cSt).

compressibility of the gas will become more important, resulting in a decrease in the scaled values of H_c again (see Langley *et al.* 2017).

Revisiting the example centreline heights from figure 2, H_c for the impact onto the liquid film was nearly 50 % larger. Now, taking into account the penetration velocity for impacts of liquid drops onto liquid surfaces, this introduces a factor of $2^{2/3}$ on the right-hand side of (3.3). Therefore, for a given impact velocity, we expect the centreline height of the air disc for impacts onto liquid surfaces to be 1.58 times the centreline height of impacts onto solid surfaces – which is in good agreement.

Figure 3(*b*) shows several air-layer profiles for a 10^5 cSt drop impacting a liquid film at $V = 1.6$ m s^{-1} ($\Phi = 7.8 \times 10^{-3}$). Time is relative to the first frame in which the deformation of the liquid interfaces was visible. As time progresses, the air layer becomes thinner and grows radially. At 50 μs, the gliding layer is ∼320 nm thick. At 100 μs, the centreline height has decreased and the drop is gliding on a layer <160 nm thick. After 200 μs, the centreline height reaches a steady value and the gliding layer extends to nearly 1000 μm. The drop continues to glide for an additional ∼300 μs before the air film ruptures. The gliding layer does not rupture at the farthest radial extent of the air layer, but at an intermediate location where the layer is close to the thinnest. For this case, the rupture occurs at $L^* = 650$ μm.

The inset of figure 3(*b*) shows the centreline height for each viscosity for an impact velocity between 1.6 and 2 m s^{-1}. At these velocities, each drop glides except the 10 cSt case, which makes ring contact at the kink when the dimple reaches its maximum height. For intermediate viscosities, 10^2 and 10^3 cSt, the dimple reaches

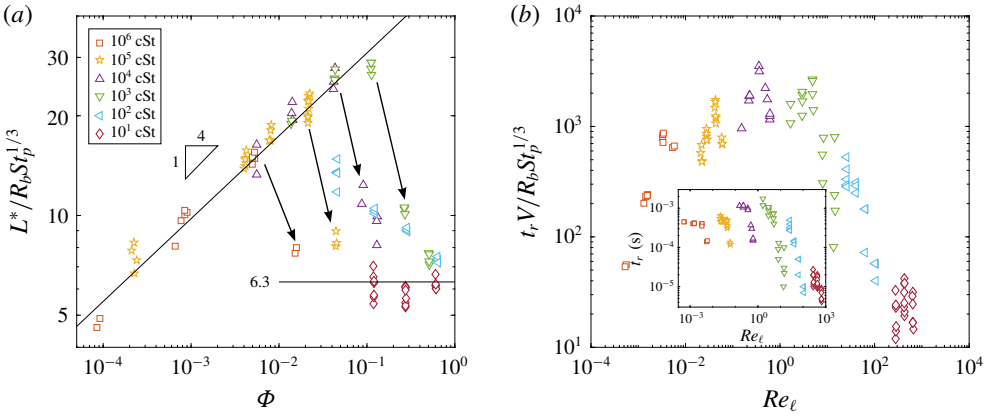

FIGURE 4. (*a*) Plot of the location of the rupture of the air layer, L^*, versus the impact parameter Φ, where L^* is normalized by Stokes-number scaling. For impacts that glide above the liquid film, the normalized radial extent of the gliding layer increases as $\Phi^{1/4}$. At sufficiently high impact velocities, there is a transition from gliding to ring contact, seen in the plot as a sudden decrease in L^* with increasing Φ. For ring contact, the rupture location approaches the radial extent predicted by Hicks & Purvis (2010) for impacts onto a solid surface (horizontal line). (*b*) Plot of non-dimensional time when the air layer ruptures versus the Reynolds number Re_ℓ. Inset: dimensional rupture time versus Reynolds number.

its maximum height and then decreases as the drop glides. Rupture occurs much faster in the 100 cSt case. As the viscosity increases further, the centreline height of the dimple gradually decreases from its maximum to a steady value that is maintained until the air layer ruptures.

3.3. *Rupture of the air layer*

The thin air layer on which the drops glide is inherently unstable and will eventually rupture when the film reaches a sufficient thinness. In our study, the air film ruptures when the film is <160 nm thick. Figure 4(*a*) shows the radial location of rupture of the air film, L^*, as a function of Φ. Here we scale L^* with Stokes-number scaling, as is common for lower-viscosity drops (Smith, Li & Wu 2003; Korobkin, Ellis & Smith 2008; Mandre *et al.* 2009; Hicks & Purvis 2011). In the gliding regime, the rupture location scales as $L^* \sim \Phi^{1/4} R_b St_p^{1/3}$, meaning that as Φ increases the gliding layers become larger. For Φ between 10^{-2} and 10^{-1}, the transition between gliding and ring contact at the kink begins. Counterintuitively, a large liquid viscosity does not equate to a larger L^*. In fact, the highest-viscosity drops begin transitioning at lower values of Φ than intermediate viscosities. This is promoted in part by a slowed spreading rate and a smaller maximum spreading radius for the highest-viscosity cases (Langley *et al.* 2017). In the plot, the transition is seen as a sharp decrease in L^*. As in the analysis for the centreline height, the penetration velocity is used in the Stokes number for the scaling of the rupture location. As Φ approaches unity, the rupture location approaches the normalized value predict by Hicks & Purvis (2010) for inviscid drop impacts onto solid surfaces (that is, $L_0 = 6.3 R_b St_p^{1/3}$). The behaviour of the rupture during the transition from gliding to ring contact at the kink is explored in more detail in § 3.5.

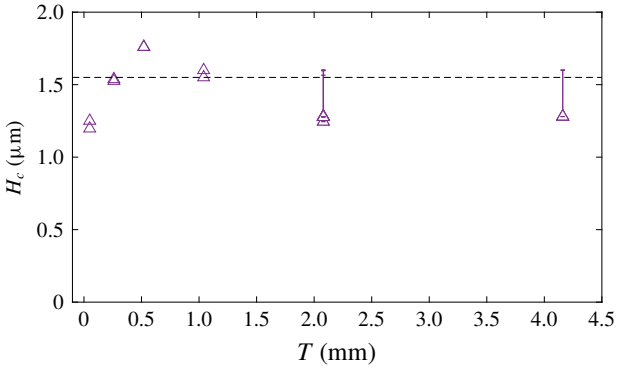

FIGURE 5. Plot of the first maximum of the centreline height of the air disc H^* versus the liquid film thickness, T, for impacts of 10^4 cSt silicone oil drops onto liquid films of the same liquid with $R_b = 1.4$ mm and $V = 1.4$ m s^{-1}.

Figure 4(*b*) shows the non-dimensional time of air film rupture, $\tau = t_r V/R_b St_p^{2/3}$, versus the Reynolds number Re_ℓ, while the inset shows the actual time. The time of rupture is measured relative to the first observed deformation of the drop. For the highest-viscosity cases 10^4–10^6 cSt, the normalized time to rupture increases with increasing velocity until the drop transitions from gliding to ring contact at the kink, at which point there is a sudden decrease in the time to rupture. Although this transition decreases τ for these cases, the rupture time is still much larger than the rupture time for the low-viscosity cases, as shown in the inset of figure 4(*b*). The time to rupture reaches a maximum near $Re_\ell = 1$, where the inertial and viscous stresses in the liquid balance. As Re_ℓ increases beyond unity, time until rupture decreases with increasing impact velocity. As the drop transitions from gliding to ring contact at the dimple edge, there is a much steeper decrease in τ with increasing Re_ℓ than for higher viscosities. In the lowest-viscosity case, 10 cSt, the time to rupture occurs at a near-constant value of $\tau \simeq 25$ or $t_r \simeq 10$ μs.

3.4. *Effects of liquid film thickness*

Hicks & Purvis (2011) present a model for inviscid drop impacts onto an inviscid liquid film with air cushioning by the intervening viscous gas. When the ratio of the liquid layer depth to the horizontal interaction distance is much greater than 1, then the liquid film can be treated as a deep pool. In our study, the liquid layer is ∼400 μm and the horizontal interaction length L is $\lesssim$300 μm when the dimple reaches its maximum height, which makes the ratio of order 1, suggesting there could be some effects from the closeness of the solid wall.

To assess the effects of the film thickness, we performed a series of experiments with 10^4 cSt silicone oil where all parameters were held constant except the film height, T, which was varied from 100 μm to 4 mm. Measurements of the centreline air-disc height H_c are plotted as a function of the film thickness in figure 5. As the film thickness increases to 500 μm, the centreline height also increases, consistent with transitioning from an effectively solid to a compliant substrate. As the substrate film thickness continues to increase, there is a slight decrease in the height until it reaches a steady value of 1.28 μm. One caveat, for film thicknesses $\leqslant$1 mm, an absolute reference measurement is clearly visible in the videos; however, for the two

thickest films there is ambiguity in the absolute thickness. If the films behave as in the lower thicknesses, the values of H_c may need to be adjusted by an additional 320 nm, as marked by the vertical bars. This must be addressed in future work using two-colour interferometry.

Where then does our data fall on the shallow film to deep pool spectrum? For the initial formation of the dimple, the behaviour of our data suggests it is on the cusp of the deep pool behaviour. As the impact continues, the solid substrate forces the drop to spread radially outwards, resulting in a flatter air film instead of the hemispherical air film seen by Thoroddsen *et al.* (2012) and Tran *et al.* (2013). Therefore, the gliding behaviour and rupture dynamics presented in our study may only be applicable when the horizontal interaction distance and the liquid film depth are of similar magnitude.

3.5. *Transition from gliding to ring contact at the kink*

Figures 6(*a*) and 6(*b*) show a drop of 10^5 cSt silicone oil impacting onto a liquid film before and after the transition from gliding to ring contact at the edge of the drop dimple. In the gliding regime just prior to transition, figure 6(*a*), the dimple forms and the drop glides for ∼350 μs before the air layer ruptures at a radial distance $L^* = 780$ μm. As the impact transitions towards ring contact at larger Φ, figure 6(*b*) shows that the drop still glides prior to rupture of the air layer. The air layer now ruptures much faster in real time after only 120 μs and ruptures near the edge of the dimple (point 1 in the last panel of figure 6*b*). At the time of rupture, the drop does not make contact with the entire liquid film simultaneously. The contact begins near the dimple and then propagates outwards. Point 2 in the last panel, marks the faintly visible outer extent of the contacted area. Point 3 shows a local contact within the still present air layer between the drop and liquid film. Aside from point 3, there is no contact between the drop and liquid film between the outer extent of the contacted region (point 2) and the outer edge of the gliding layer, which is the furthest radially the drop has spread (right facing arrow). The outer edge of the contacted region will continue to spread outwards, entrapping microbubbles as it propagates. Li, Vakarelski & Throddsen (2015) showed similar film ruptures for water drops impacting a film of 2×10^7 cSt silicone oil.

Figure 6(*c*) shows this transition for 100 cSt drops from gliding to contact at the kink. Each panel shows the rupture location for a different impact velocity, increasing from left to right. These frames also correspond to the light blue triangles that are trending downwards and to the right in figure 4. As the impact velocity increases, the rupture location moves progressively closer to the edge of the dimple until at a sufficiently high impact velocity, $V = 3.8$ m s^{-1}, the drop makes contact at the kink. Unlike in the cases with higher viscosity, the lower-viscosity drop does not first glide for a large distance and then later rupture near the kink as in figure 6(*b*). The contact is made at the kink, before the drop begins to spread outwards.

3.6. *Contraction of the air film*

When fluid films rupture within viscous outer fluids, the retraction velocity V_r is typically dictated by balancing the capillary and viscous forces. Reyssat & Quéré (2006) studied the bursting of thin films and proposed a logarithmic correction to a simple capillary–viscous balance, σ/μ_ℓ, for the retraction velocity of the edge

$$V_r = \frac{\sigma}{2\pi\mu_\ell} \ln\left(\frac{4\mu_\ell}{\rho_\ell V_r r}\right), \tag{3.4}$$

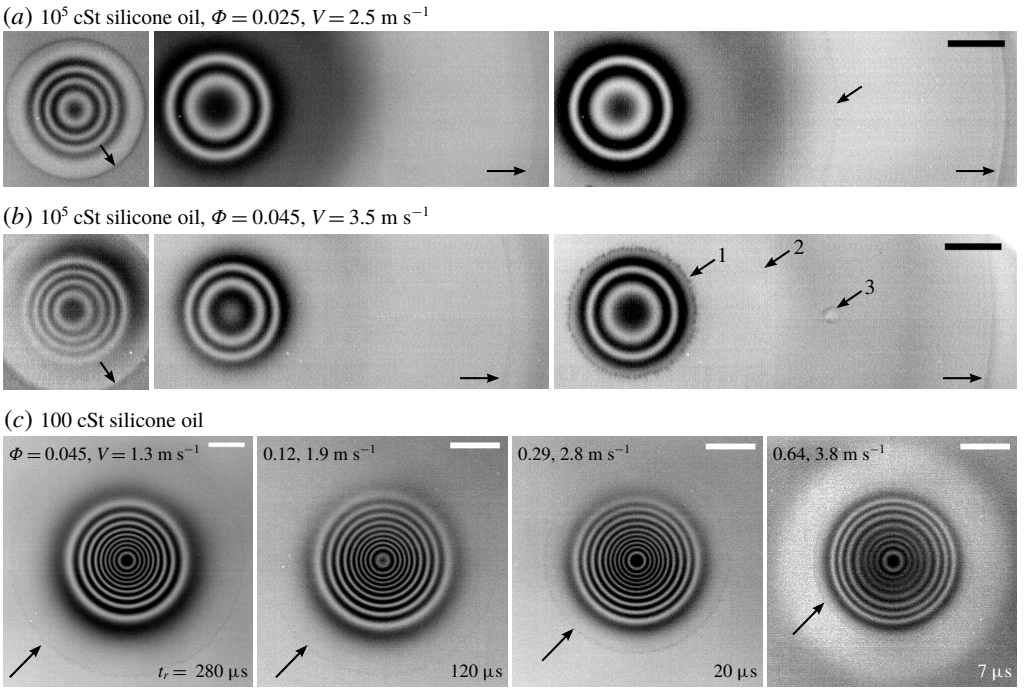

FIGURE 6. Bottom-view interferometry images showing the transition from gliding to ring contact at the kink. Image intensities have been inverted to better show the details at the rupture location. (*a*) A drop of 10^5 cSt silicone oil impacting in the gliding regime, shown at 0, 185 and 375 μs relative to the first frame which shows the dimple. The right-facing arrows show the furthest that the drop has spread radially (that is, the extent of the region where a thin air layer separates the drop and substrate liquid film). In the last panel the drop has spread to ∼75 % of R_b. The drop has not yet contacted the liquid film in the middle panel. The left-facing arrow in the last panel shows the rupture location of the thin air layer. (*b*) The impact of a drop of 10^5 cSt silicone oil under conditions at the transition between gliding and ring contact at the kink, shown at 0, 80 and 160 μs relative to the first frame showing the dimple. The right-facing arrows show the furthest extent of the drop spreading. The drop initially glides over a thin layer of air and has not yet contacted the liquid film in the middle panel. The air layer ruptures near the edge of the dimple in the drop (point 1). The outer edge of the rupture can be faintly seen at point 2, and point 3 shows a localized contact in the still present air layer. The outer rupture propagates towards the outer edge, leaving a myriad of microbubbles. (*c*) Bottom-view images for impacts of 100 cSt silicone oil onto a liquid film of the same liquid at different impact velocities. The arrows show the location of the rupture of the thin air film upon which the drop initially glides. For increasing Φ (increasing V) the rupture location moves closer to the initial kink at the edge of the drop dimple until the contact occurs at the kink as for impacts onto solid surfaces. Each Φ value corresponds with a blue triangle in figure 4. Each scale bar is 200 μm long.

where r is the radius of the rim of the retracting fluid, which is on the order of the thickness of the film when it first bursts. Figure 7(*a*) shows the average measured retraction velocity of the extended air film versus liquid viscosity compared with (3.4). Here we have taken $r = 160$ nm. For the low-viscosity cases, V_r follows the expected behaviour; however, for $\mu_\ell > 10^2$ cSt the retraction velocity is nearly

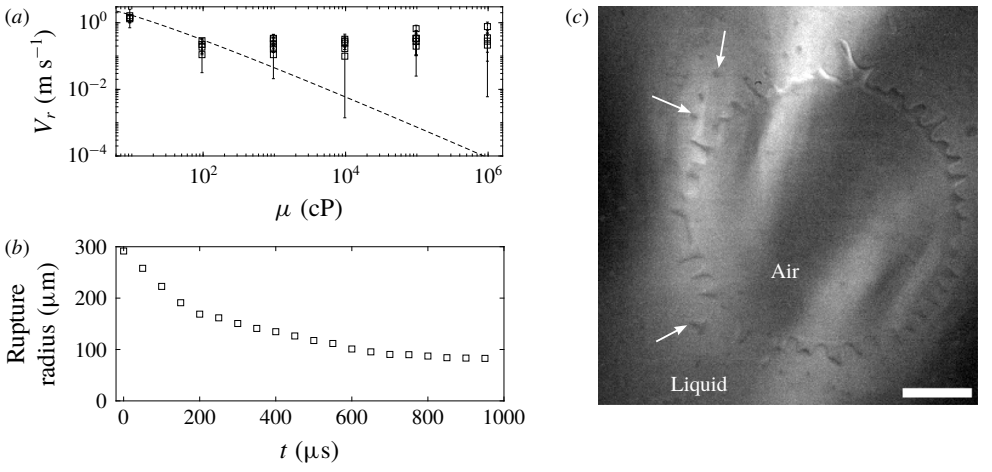

FIGURE 7. (*a*) Retraction velocity of the air film after rupture. The dotted line is the predicted velocity from Reyssat & Quéré (2006) given in (3.4). (*b*) Radius versus time for a retracting air film in 10^6 cSt silicone oil. (*c*) Bottom-view image, with lighting from above, of a retracting air film entrapped in 10^6 cSt silicone oil. White arrows mark microbubbles that were entrained as the film retracts. The drop initially impacted at $V = 1.7$ m s^{-1}. The scale bar is 200 μm.

constant at 0.28 m s^{-1}. We suspect that the deviation is due to the thinness of the air film when rupture occurs being two orders of magnitude smaller than those studied by Reyssat & Quéré (2006). For drop impacts onto solid surfaces where a similar thickness air layer exists, Langley *et al.* (2017) measured contact line velocities to be independent of viscosity for the localized contacts within the gliding layer for μ_ℓ as high as 2×10^7 cSt. At these thicknesses, perhaps the wetting behaviour is not solely due to a moving sharp edge and the liquid instead could be making contact by vertically draping over the surface or perhaps assisted by van der Waals forces when the thickness is on the order of 10 nm. The thickness of the air films is also of the same order as the mean free path of the air molecules, which may lead to possible rarefied gas effects that may enhance the wetting speed (see Li *et al.* 2017).

For contracting central air discs, the retraction velocity varies in time. The instantaneous initial retraction velocities can be much greater than the average velocity. Figure 7(*b*) shows the radius of a retracting air film within 10^6 cSt silicone oil versus time, with $t = 0$ corresponding to the time of rupture. The initial velocity is 0.7 m s^{-1}, which slows to an average value of 0.11 m s^{-1} after 200 μs. This drastic slow down corresponds with the edge of the retracting film reaching the outer edge of the much thicker central dimple.

Figure 7(*c*) shows a bottom-view image of an air film retracting in 10^6 cSt silicone oil. As the air film contracts, the rim of the film becomes unstable, forming a series of tips around the periphery. As the film continues to retract, the tips are pinched off, forming myriad microbubbles, as shown by the arrows in the figure. As the film radius decreases, the number of tips around the periphery also decreases.

4. Conclusions

Herein, we have investigated the early impact dynamics of high-viscosity drops impacting onto films of the same liquid. As the drop approaches the liquid surface,

the pressure in the intervening gas layer rises, deforming both the drop and film interfaces by the amount corresponding to an effective velocity equal to 1/2 of the impact velocity. Using this approach velocity in the Stokes number, St_p, unifies the scaling for the centreline height of the air disc for highly viscous drop impacts onto solid and liquid surfaces. In both cases the normalized initial centreline height, H_c, scales with the impact parameter, $\Phi = (\rho_\ell V^2/P_{atm})Re_\ell^{1/3}$, to the 1/3 power, revealing a weak dependence on liquid viscosity, $\sim\mu_\ell^{-1/9}$.

For small Φ, the drop does not initially make contact with the liquid film but instead glides on a thin layer of air. The normalized radial extent of the gliding layer increases as $\Phi^{1/4}$. For increasing Φ, the drop transitions from gliding to ring contact at the kink on the edge of the central dimple. The transition is demarcated by a sudden decrease in the radial location of the rupture of the thin extended air layer. The time from dimple formation to air film rupture also decreases suddenly.

Overall, the time at rupture behaves non-monotonically as a function of Re_ℓ. For liquid viscosities greater than 10^3 cSt, there is an increase in the time to rupture with increasing Re_ℓ, as $Re_\ell \to 1$ from below. For the smaller liquid viscosities, the time to rupture decreases with increasing Re_ℓ.

As $\Phi \to 1$, both the centreline height and rupture location approach the values expected for inviscid drop impacts onto solid surfaces. For lower-viscosity drops, the air film contracts after rupture according to established theory; however, for liquid viscosity $>10^2$ cSt the air film contracts with a near-constant velocity independent of viscosity.

It remains to study in more detail how the thickness of the liquid film influences the thickness of the entrapped air layer. Figure 5 shows this trend only for one viscosity of 10^4 cSt. Intuitively one may expect that the depth will be less important at higher viscosities, as the deformations become much smaller; however, a higher liquid viscosity could result in the presence of the wall being felt over larger distances.

Acknowledgement

The work reported herein was funded by King Abdullah University of Science and Technology (KAUST) under grant URF/1/3727-01-01.

Supplementary materials

Supplementary materials are available at https://doi.org/10.1017/jfm.2019.682.

References

BOUWHUIS, W., VAN DER VEEN, R. C. A., TRAN, T., KEIJ, D. L., WINKELS, K. G., PETERS, I. R., VAN DER MEER, D., SUN, C., SNOEIJER, J. H. & LOHSE, D. 2012 Maximal air bubble entrainment at liquid-drop impact. *Phys. Rev. Lett.* **109**, 264501.

BOUWHUIS, W., HUANG, X., CHAN, C. U., FROMMHOLD, P. E., OHL, C.-D., LOHSE, D., SNOEIJER, J. H. & VAN DER MEER, D. 2016 Impact of a high-speed train of microdrops on a liquid pool. *J. Fluid Mech.* **792**, 850–868.

CROOKS, J., MARSH, B., TURCHETTA, R., TAYLOR, K., CHAN, W., LAHAV, A. & FENIGSTEIN, A. 2013 Kirana: a solid-state megapixel uCMOS image sensor for ultrahigh speed imaging. *Proc. SPIE* **8659**, 865903.

HENDRIX, M. H. W., BOUWHUIS, W., VAN DER MEER, D., LOHSE, D. & SNOEIJER, J. H. 2016 Universal mechanism for air entrainment during liquid impact. *J. Fluid Mech.* **789**, 708–725.

HICKS, P. D. & PURVIS, R. 2010 Air cushioning and bubble entrapment in three-dimensional droplet impacts. *J. Fluid Mech.* **649**, 135–163.

HICKS, P. D. & PURVIS, R. 2011 Air cushioning in droplet impacts with liquid layers and other droplets. *Phys. Fluids* **23** (6), 062104.

HOWISON, S. D., OCKENDON, J. R., OLIVER, J. M., PURVIS, R. & SMITH, F. T. 2005 Droplet impact on a thin fluid layer. *J. Fluid Mech.* **542**, 1–23.

JOSSERAND, C. & ZALESKI, S. 2003 Droplet splashing on a thin liquid film. *Phys. Fluids* **15**, 1650–1657.

JOSSERAND, C. & THORODDSEN, S. T. 2016 Drop impact on a solid surface. *Annu. Rev. Fluid Mech.* **48**, 365–391.

KOLINSKI, J. M., MAHADEVAN, L. & RUBINSTEIN, S. M. 2014*a* Drops can bounce from perfectly hydrophilic surfaces. *Eur. Phys. Lett.* **108**, 24001.

KOLINSKI, J. M., MAHADEVAN, L. & RUBINSTEIN, S. M. 2014*b* Lift-off instability in the impact of a drop on a solid surface. *Phys. Rev. Lett.* **112**, 134501.

KOLINSKI, J. M., RUBINSTEIN, S. M., MANDRE, S., BRENNER, M. P., WEITZ, D. A. & MAHADEVAN, L. 2012 Skating on a film of air: drops impacting on a surface. *Phys. Rev. Lett.* **108**, 074503.

KOROBKIN, A. A., ELLIS, A. S. & SMITH, F. T. 2008 Trapping of air in impact between a body and shallow water. *J. Fluid Mech.* **611**, 365–394.

LANGLEY, K., LI, E. Q. & THORODDSEN, S. T. 2017 Impact of ultra-viscous drops: air-film gliding and extreme wetting. *J. Fluid Mech.* **813**, 647–666.

LANGLEY, K. R., LI, E. Q., VAKARELSKI, I. U. & THORODDSEN, S. T. 2018 The air entrapment under a drop impacting on a nano-rough surface. *Soft Matt.* **14**, 7586–7596.

LI, E. Q., LANGLEY, K. R., TIAN, Y. S., HICKS, P. D. & THORODDSEN, S. T. 2017 Double contact during drop impact on a solid under reduced air pressure. *Phys. Rev. Lett.* **119**, 214502.

LI, E. Q. & THORODDSEN, S. T. 2015 Time-resolved imaging of compressible air disc under drop impacting a solid surface. *J. Fluid Mech.* **780**, 636–648.

LI, E. Q., VAKARELSKI, I. U. & THRODDSEN, S. T. 2015 Probing the nano-scale: the first contact of an impacting drop. *J. Fluid Mech.* **785**, R2.

MANDRE, S., MANI, M. & BRENNER, M. P. 2009 Precursors to splashing of liquid droplets on a solid surface. *Phys. Rev. Lett.* **102**, 134502.

MARSTON, J. O., VAKARELSKI, I. U. & THORODDSEN, S. T. 2011 Bubble entrapment during sphere impact onto quiescent liquid surfaces. *J. Fluid Mech.* **680**, 660–670.

PHILIPPI, J., LAGRÉE, P.-Y. & ANTKOWIAK, A. 2016 Drop impact on a solid surface: short-time self-similarity. *J. Fluid Mech.* **795**, 96–135.

REYSSAT, E. & QUÉRÉ, D. 2006 Bursting of a fluid film in a viscous environment. *Europhys. Lett.* **76** (2), 236–242.

DE RUITER, J., OH, J. M., VAN DEN ENDE, D. & MUGELE, F. 2012 Dynamics of collapse of air films in drop impact. *Phys. Rev. Lett.* **108**, 074505.

DE RUITER, J., VAN DEN ENDE, D. & MUGELE, F. 2015 Air cushioning in droplet impact. II. Experimental characterization of the air film evolution. *Phys. Fluids* **27**, 012105.

SMITH, F. T., LI, L. & WU, G. X. 2003 Air cushioning with a lubrication/inviscid balance. *J. Fluid Mech.* **482**, 291–318.

SPEIRS, N. B., PAN, Z., BELDEN, J. & TRUSCOTT, T. T. 2018 The water entry of multi-droplet streams and jets. *J. Fluid Mech.* **844**, 1084–1111.

TANG, X., SAHA, A., LAW, C. K. & SUN, C. 2018 Bouncing-to-merging transition in drop impact on liquid film: role of liquid viscosity. *Langmuir* **34**, 2654–2662.

THORODDSEN, S. T. 2002 The ejecta sheet generated by the impact of a drop. *J. Fluid Mech.* **451**, 373–381.

THORODDSEN, S. T., TAKEHARA, K. & ETOH, T. G. 2003 Air entrapment under an impacting drop. *J. Fluid Mech.* **478**, 125–134.

THORODDSEN, S. T., TAKEHARA, K., ETOH, T. G., OOTSUKA, N. & HATSUKI, Y. 2005 The air bubble entrapped under a drop impacting a solid surface. *J. Fluid Mech.* **545**, 203–212.

THORODDSEN, S. T., THORAVAL, M.-J., TAKEHARA, K. & ETOH, T. G. 2011 Droplet splashing by a slingshot mechanism. *Phys. Rev. Lett.* **106**, 034501.

THORODDSEN, S. T., THORAVAL, M.-J., TAKEHARA, K. & ETOH, T. G. 2012 Micro-bubble morphologies following drop impacts onto a pool surface. *J. Fluid Mech.* **708**, 469–479.

TRAN, T., DE MALEPRADE, H., SUN, C. & LOHSE, D. 2013 Air entrainment during impact of droplets on liquid surfaces. *J. Fluid Mech.* **726**, R3.

VAN DER VEEN, R. C. A., TRAN, T., LOHSE, D. & SUN, C. 2012 Direct measurements of air layer profiles under impacting droplets using high-speed color interferometry. *Phys. Rev.* E **85**, 026315.

YARIN, A. L. 2006 Drop impact dynamics: splashing, spreading, receding, bouncing. *Annu. Rev. Fluid Mech.* **38**, 159–192.